

## Article

# Thermal Characterization and Preclinical Feasibility Verification of an Accessible, Carbon Dioxide-Based Cryotherapy System

Yixin Hu <sup>1</sup>, Naomi Gordon <sup>1</sup>, Katherine Ogg <sup>1</sup>, Dara L. Kraitchman <sup>2</sup>, Nicholas J. Durr <sup>3</sup> and Bailey Surtees <sup>1,\*</sup>

<sup>1</sup> Kubanda Cryotherapy, Inc., Baltimore, MD 21211, USA; clarisse@kubandacryo.com (Y.H.); naomi@kubandacryo.com (N.G.); katie@kubandacryo.com (K.O.)

<sup>2</sup> Department of Radiology and Radiological Science, Johns Hopkins University, Baltimore, MD 21205, USA; dkraitc1@jhmi.edu

<sup>3</sup> Department of Biomedical Engineering, Johns Hopkins University, Baltimore, MD 21218, USA; ndurr@jhu.edu

\* Correspondence: bailey@kubandacryo.com

**Abstract:** To investigate the potential of an affordable cryotherapy device for the accessible treatment of breast cancer, the performance of a novel carbon dioxide-based device was evaluated through both benchtop testing and an in vivo canine model. This novel device was quantitatively compared to a commercial device that utilizes argon gas as the cryogen. The thermal behavior of each device was characterized through calorimetry and by measuring the temperature profiles of iceballs generated in tissue phantoms. A 45 min treatment in a tissue phantom from the carbon dioxide device produced a  $1.67 \pm 0.06$  cm diameter lethal isotherm that was equivalent to a 7 min treatment from the commercial argon-based device, which produced a  $1.53 \pm 0.15$  cm diameter lethal isotherm. An in vivo treatment was performed with the carbon dioxide-based device in one spontaneously occurring canine mammary mass with two standard 10 min freezes. Following cryotherapy, this mass was surgically resected and analyzed for necrosis margins via histopathology. The histopathology margin of necrosis from the in vivo treatment with the carbon dioxide device at 14 days post-cryoablation was 1.57 cm. While carbon dioxide gas has historically been considered an impractical cryogen due to its low working pressure and high boiling point, this study shows that carbon dioxide-based cryotherapy may be equivalent to conventional argon-based cryotherapy in size of the ablation zone in a standard treatment time. The feasibility of the carbon dioxide device demonstrated in this study is an important step towards bringing accessible breast cancer treatment to women in low-resource settings.

**Keywords:** breast cancer; cryotherapy; global health; calorimetry; thermal analysis



**Citation:** Hu, Y.; Gordon, N.; Ogg, K.; Kraitchman, D.L.; Durr, N.J.; Surtees, B. Thermal Characterization and Preclinical Feasibility Verification of an Accessible, Carbon Dioxide-Based Cryotherapy System. *Bioengineering* **2024**, *11*, 391. <https://doi.org/10.3390/bioengineering11040391>

Academic Editors: Brian T. Crouch and Jenna Mueller

Received: 1 March 2024

Revised: 5 April 2024

Accepted: 12 April 2024

Published: 18 April 2024



**Copyright:** © 2024 by the authors. Licensee MDPI, Basel, Switzerland. This article is an open access article distributed under the terms and conditions of the Creative Commons Attribution (CC BY) license (<https://creativecommons.org/licenses/by/4.0/>).

## 1. Introduction

Breast cancer is the most diagnosed cancer, with more than 2.3 million new cases each year, representing nearly a quarter of all cancer diagnoses in women [1]. Over 60% of breast cancer cases occur in low-and-middle-income countries (LMICs) and account for 70% of all breast cancer deaths [1]. Breast cancer has become one of the leading causes of morbidity and mortality in LMICs. In high-income countries, such as the U.K., U.S., Canada, and Northern Europe, women have an 85% five-year survival rate, compared to 50% in LMICs [2]. Major causes of this disparity are the geographic and socioeconomic constraints that limit access to standard healthcare facilities and treatments [3]. For many women, socioeconomic status creates a significant barrier to seeking proper care [2].

The current standard-of-care treatments for breast cancer in high-resource countries include surgery, chemotherapy, and radiation. Unfortunately, these treatments are costly and often unavailable to women in low-resource settings [4]. Chemotherapy and radiation require expensive drugs, complex equipment, and robust supply chains. Surgical options, such as lumpectomy and mastectomy, require sterile operating rooms and surgical expertise that are not widely available in local clinics in LMICs. Globally, access to appropriate

surgical care is alarmingly limited, with less than 25% of the population having access [5] and only 10% of LMICs having access to the 25 cancer medications on the WHO Model Lists of Essential Medicines [6]. Nearly 50% of African countries completely lack radiotherapy equipment [7]. In low-income countries, there is an average of one radiotherapy device per 7 million people, compared to high-income countries where there is one per 250,000 [8]. Aside from the restricted access to necessary resources for standard care, breast cancer patients in LMICs seeking treatment also face a significant financial burden, with average expenses of USD 1300 for surgery, USD 1400 for chemotherapy, and USD 1200 for radiation therapy [9].

Many LMICs are now promoting and adopting nationwide breast cancer screening programs [3,10], and, due to key patent expirations [11,12], affordable breast cancer diagnostics, such as handheld ultrasound and low-cost mammography, are now emerging [13–15]. However, despite advances in early detection, few affordable treatments are available to address the breast cancer burden in LMICs.

Cryotherapy is an established treatment method for many benign and malignant tumors and has been used since the 1970s in various cancer types, including prostate, kidney, liver, and lung cancer [16,17]. During the procedure, extreme cold is delivered via a probe to necrose cancerous tissue, and the body's immune system subsequently breaks down the dead cells. Cryoablation is typically performed under local anesthesia with minimal sedation. Due to the small, minimally invasive cryoprobe and the analgesic properties of cold, the procedure can be performed percutaneously under image guidance for deep organs and only leaves a scab at the treatment site. However, existing commercial cryotherapy systems are not feasible for use in LMICs due to their reliance on expensive and inaccessible cryogens such as liquid nitrogen and argon gas. These gases necessitate specialized safe handling protocols, and using the systems also demands extensive specialized training to navigate their complex operating systems. Systems can cost upwards of USD 250,000 per unit [18] and more than USD 5000 in single-use disposables per treatment [19].

This study investigates a carbon dioxide-based cryotherapy device by benchmarking its thermal performance against a commercially available argon-based system in both a calorimeter system and in tissue phantoms. Additionally, an *in vivo* verification was conducted in a canine model to demonstrate proof-of-concept for future human studies with the device. This CO<sub>2</sub> cryotherapy device meets many of the criteria for treating breast cancer in LMICs, including affordability, ease of use, and operation without electricity. While CO<sub>2</sub> is low-cost and abundantly available due to its use in the beverage industry, its use as a cryogen is considered limited because of its higher boiling point at  $-78.46\text{ }^{\circ}\text{C}$  as compared to more costly cryogens, like liquid nitrogen and argon gas, which have boiling points of  $-195.8\text{ }^{\circ}\text{C}$  and  $-185.8\text{ }^{\circ}\text{C}$ , respectively. CO<sub>2</sub> also has a lower working pressure of around 860 psi as compared to argon gas, which is used at around 3000–4500 psi in cryotherapy systems [20]. Because the operating principle of most cryotherapy devices, the Joule–Thomson effect, involves the throttling of a cryogen from high to low pressure, the lower working pressure of CO<sub>2</sub> limits its cryogenic potential.

Low-cost cryotherapy based on cheaper cryogens such as gaseous and solid CO<sub>2</sub> was explored during the early cryotherapy development of the mid-1900s, but interest in this technology decreased with the advent of liquid nitrogen- and argon-based systems [21]. Lower-boiling-point and higher-pressure cryogens allow for faster cooling, and as the per-minute operating room costs increased, shorter treatment times were prioritized for cost-effectiveness.

In prior work, the CO<sub>2</sub> device has undergone engineering optimizations, including cryoprobe geometry and a gas pre-cooling system, to fully harness the cooling power of gaseous CO<sub>2</sub>. Usability considerations were further implemented to make the device compatible with beverage- and food-grade CO<sub>2</sub>. The device's efficacy in necrosing cancerous tissue and creating a clinically relevant-sized iceball under heat load has been previously validated in rat mammary tumors and swine liver, respectively [22].

This research adds to the previous work by conducting a benchmark study comparing the thermal performance of the CO<sub>2</sub> device to a commercial argon-based system, and by verifying the efficacy of the CO<sub>2</sub> device under heat load in a spontaneously occurring tumor in a large animal model. In this study, the CO<sub>2</sub> device's thermal performance was quantitatively compared to that of an argon-based cryotherapy system through bench tests, particularly the ability to reach similar freezing outcomes under heat load. First, a calorimeter test was performed for both devices to determine the total power output. Then, a bench test in tissue phantom simulating the human body's thermal properties and heat load conditions was completed to evaluate the time efficiency in forming a clinically relevant-sized iceball and to measure the lethal isotherm margins. Finally, one in vivo treatment using the CO<sub>2</sub> device was completed in a client-owned dog with a spontaneously occurring mammary tumor to confirm the device's ability to necrose cancerous tissue under physiological heat load in a spontaneously occurring tumor in a large animal model.

## 2. Materials and Methods

### 2.1. Device Comparison

This study compares the thermal performance and cooling efficiency of a novel CO<sub>2</sub>-based cryotherapy device to a commercially available benchmark argon-based device indicated for use in human therapeutic applications. The metric used in this study to evaluate the ability of a cryotherapy device to induce cell death is a  $-20\text{ }^{\circ}\text{C}$  isotherm. The size of the  $-20\text{ }^{\circ}\text{C}$  isotherm generated by a cryotherapy device during treatment is widely accepted to correlate with the lethal zone in tissue [23–25]. Although CO<sub>2</sub> cannot reach temperatures as low as argon due to its inherent thermal characteristics, it is still an effective cryogen, as its boiling point is significantly below the lethal temperature of  $-20\text{ }^{\circ}\text{C}$ , making it an appropriate cryogen for many applications.

The CO<sub>2</sub> device is entirely mechanical, consisting of a gas-regulating backend unit that directly connects to a standard pressurized CO<sub>2</sub> tank. The device is operated by a simple on-off valve that controls the flow of gas to the system. High-pressure tubing connects the gas-regulating backend to a handle composed of two concentric tubes: a telescoping nozzle that throttles the incoming high-pressure CO<sub>2</sub>, and a larger pre-cooling chamber through which cooled, expanded gas is directed back to the backend and exhausted into the environment. An 8-gauge aluminum probe (Figure 1) is connected to the handle to conduct cold into the targeted treatment volume, generating an iceball and inducing tissue necrosis.

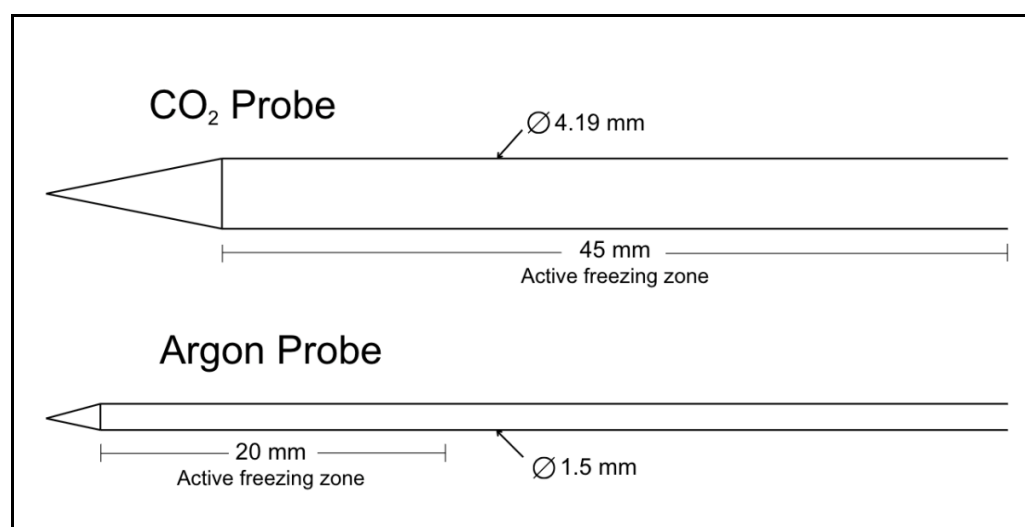


**Figure 1.** A comparison of the cryoprobe size, shape, and active freezing zone profiles is shown for the two devices. The CO<sub>2</sub> device has a probe diameter of 4.19 mm, while the benchmark argon device has a probe diameter of 1.50 mm.

The benchmark argon device (Galil Medical, SeednetSystem, IceSeed probe, Shaar Yokneam, Israel) has a 17-gauge single-use stainless steel probe (Figure 1). Published performance specifications report its ability to generate a 2 cm diameter iceball with a  $-20\text{ }^{\circ}\text{C}$  1.5 cm diameter isotherm, corresponding to the lethal zone during treatment. The benchmark device has an electronic control module for gas regulation and an active thaw feature that utilizes helium gas to warm the probe between freeze cycles [26]. Both devices have sharp-tipped probes designed to be inserted directly into the targeted tissue without the use of a scalpel.

Because of the difference in probe sizes of the two devices, methods of correction were introduced into each experiment to directly compare the thermal performance of the two devices.

The primary focus of this study is to establish the thermal performance of the  $\text{CO}_2$  device in comparison to a commercial device and to demonstrate that the  $\text{CO}_2$  device can induce clinically significant margins of necrosis in cancerous tissue in a spontaneously occurring tumor in a large animal model under heat load.

## 2.2. Calorimeter Testing

The calorimeter setup consisted of two nested aluminum vessels, separated by insulating foam and sealed with an insulating lid. The inner cup was filled with 155 g of water at  $65\text{ }^{\circ}\text{C}$ , and a stir bar was used continuously to ensure an even temperature distribution. To monitor the water temperature, a 40-gauge type-T thermocouple with PFA insulation (Omega Engineering, Norwalk, CT, USA) was fixed inside the internal vessel. Temperature data were recorded using a data logging thermometer (Omega Engineering, RDXL4SD). Before experimentation, the thermocouples were calibrated in accordance with the manufacturer's instructions against reference points of ice water and boiling water.

Three 140 s freezing trials were performed with each cryoprobe. During the trial, the cryoprobe was inserted into the calorimeter and allowed to freeze for 140 s. The temperature inside the calorimeter was recorded every 20 s. After each trial, the initial conditions were reset by re-establishing the water temperature to  $65\text{ }^{\circ}\text{C}$ . The rate of change in temperature within the calorimeter was used to compute the cryoprobe's cooling power,  $P$ , in Watts using the thermal energy equation,

$$P = \frac{m_c \Delta T}{t}, \quad (1)$$

where  $m$  is the mass of the water in the calorimeter,  $C_p$  is the specific heat capacity of water ( $4.184\text{ J/g}^{\circ}\text{C}$ ),  $\Delta T$  is the change in temperature, and  $t$  is the time interval. The cooling powers measured from each of the three intervals were averaged to calculate the overall cooling power of the cryoprobe.

The cooling power over the surface area of the active freezing zone was normalized between the two systems to correct for the differences in probe size.

## 2.3. Tissue Phantom with Heat Load Testing

### 2.3.1. Tissue Phantom

A benchtop tissue phantom was developed to simulate the thermal conditions of tissue during a cryotherapy treatment. A beaker containing 234 g of ultrasound gel was heated to  $37\text{ }^{\circ}\text{C}$  and placed in a heated water bath that circulated at  $37\text{ }^{\circ}\text{C}$  to simulate the heat load and perfusion conditions of a body with a constant core temperature (Figure 2).

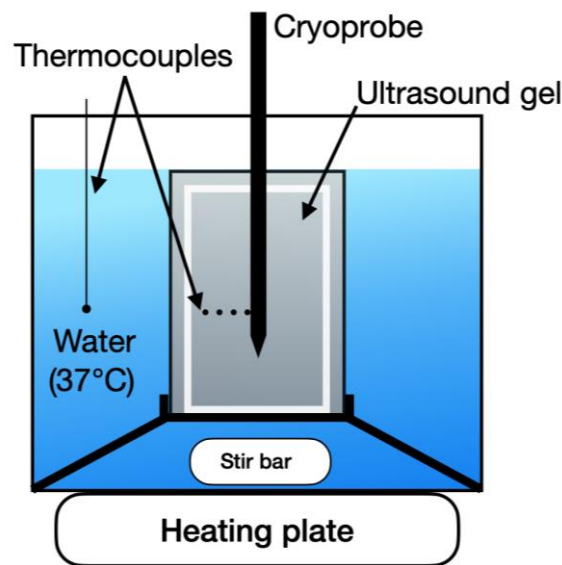


**Figure 2.** Tissue phantom testing setup. The cryoprobe is placed in a custom fixture containing heated ultrasound gel with four thermocouples at fixed radial distances from the probe surface. The ultrasound gel is surrounded by a 37 °C water bath maintained with temperature monitoring and control, simulating the heat load conditions of a body.

A fixture centered the probe in the ultrasound gel and held the thermocouples at fixed radial intervals. To account for the difference in diameter between the CO<sub>2</sub> probe (4.19 mm) and the argon probe (1.5 mm), a separate fixture was designed for each probe, and temperature measurements were taken at equivalent distances of 1 mm, 4 mm, 7 mm, and 10 mm from each probe’s outer surface (Figure 3) by recording with a 0.5 Hz sampling rate.

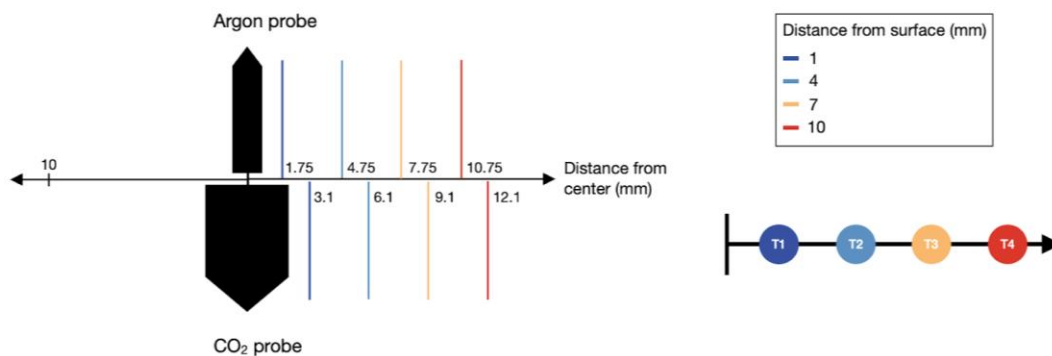


**Figure 3.** Positions of the four thermocouples. Left: a comparison of the center distance of the thermocouples for the argon and CO<sub>2</sub> probes. Right: a diagram showing the distance of each thermocouple from the probe surface.

Preliminary tests were performed to determine the specific vertical position on each probe corresponding to the maximum diameter of the iceball. The thermocouple fixture was then aligned with this position during subsequent testing. Additionally, a fifth thermocouple was positioned 1 cm away from the probe’s center to monitor the time for the iceball to achieve a 2 cm diameter (Figure 3).

To measure an isotherm of clinically relevant size, the testing duration ranged from 7 min for the argon device to 45 min for the CO<sub>2</sub> device. A total of 10 trials were conducted for each probe, and the temperature distributions were evaluated by using Matlab. Minor fluctuations in the temperature data were smoothed with second-degree Savitzky–Golay filtering [27].

### 2.3.2. Mathematical Modeling

The tissue phantom study aimed to determine the size of the  $-20\text{ }^{\circ}\text{C}$  isotherm for each device after a specified testing period. Because temperature values were recorded at discrete thermocouple locations, a curve-fitting model was used to approximate the temperature values across the entire iceball diameter perpendicular to the probe.

The tissue phantom was designed to simulate the thermal properties and heat load conditions of human tissue. To evaluate the theoretical temperature distribution in the tissue phantom, we began with Pennes' bioheat equation, which models the thermal dynamics within biological tissues:

$$\frac{1}{r^2} \frac{d}{dr} \left( r^2 \frac{dT}{dr} \right) + \frac{w_b c_b}{k} (T_a - T) + \frac{q_m}{k} = 0, \quad (2)$$

where  $r$  is the radius from an infinitesimal point source of cooling,  $w_b$  is the perfusion rate per unit volume of blood,  $c_b$  is the specific heat of blood,  $k$  is the thermal conductivity of tissue,  $T$  is the tissue temperature,  $T_a$  is the arterial temperature, and  $q_m$  is the metabolic heat generation per unit volume [28].

In the experimental tissue phantom, metabolic heat, arterial blood heating, and blood perfusion were not simulated, which reduces the bioheat equation to a simple conduction equation:

$$\frac{1}{r^2} \frac{\partial}{\partial r} \left( r^2 \frac{\partial T}{\partial r} \right) + Q = 0. \quad (3)$$

Solving this conduction equation in 1-dimensional cylindrical coordinates results in an equation of the following form:

$$T(r) = C_1 \ln(r) + C_2, \quad (4)$$

where  $C_1$  and  $C_2$  are constants [29].

The temperatures measured by each of the four thermocouples were averaged over 10 trials, and the temperature data at the end time points of the testing periods were evaluated as steady-state temperature distributions. A curve of the mathematical form in Equation (4) was fit to the four data points. The distance of the  $-20\text{ }^{\circ}\text{C}$  isotherm from the probe surface was determined from the best-fit curve.

To analyze the variation in temperature performance of the probes, the 95% confidence intervals of the temperature data from each thermocouple were computed. The curves of the mathematical form in Equation (4) were fitted to the upper and lower confidence interval bounds, and the points where each fitted curve intersected the  $-20\text{ }^{\circ}\text{C}$  isotherm were determined.

## 2.4. In Vivo Testing

### 2.4.1. Cryotherapy Procedure in a Canine Model with Spontaneously Occurring Mammary Cancer

The animal study protocol was approved by the Animal Care and Use Committee at Johns Hopkins University, and informed consent was obtained from the dog's owner. The efficacy of the  $\text{CO}_2$  cryoablation device was verified in a 9-year-old 7.8 kg mixed-breed dog presenting with a  $\sim 2.5$  cm cystic mass on the right cranial mammary gland. A fine-needle aspirate confirmed that the mass was an epithelial neoplasia with inflammation and cystic formation.

The dog was sedated with fentanyl ( $5\text{ }\mu\text{g}/\text{kg}$  IV) and received maropitant citrate ( $1\text{ mg}/\text{kg}$  IV) as an anti-nausea medication. The dog was then inducted with midazolam ( $0.25\text{ mg}/\text{kg}$  IV) followed by propofol ( $4\text{ mg}/\text{kg}$  IV). The dog was intubated, and general anesthesia was maintained with isoflurane by using mechanical ventilation at  $\sim 12$ – $15$  breaths per minute. Physiological monitoring parameters during the procedure included temperature, blood pressure, ECG, oxygen saturation, and end-tidal carbon dioxide.

The dog was shaved, sterilely prepped, and draped, and the cryoprobe was inserted into the mass (Figure 4). Sterile saline was injected between the mass and skin to displace the skin as a preventative for cold damage to the skin. A small stab incision was made into the skin prior to the insertion of the CO<sub>2</sub> cryoablation probe. Following the recommended treatment dosage for a 3 cm mass given for both the CO<sub>2</sub> device and the argon device, the cryoablation procedure was performed with two 10 min freeze periods separated by a 7 min passive thaw period. Throughout the procedure, the surgical site was observed for signs of cold damage to the skin, and the mass was manually palpated to monitor iceball growth. Ultrasound gel was placed on the skin and at the probe entry site, and room-temperature sterile saline was used to irrigate the skin to prevent thermal damage to healthy skin. After the probe was removed, the entry site was closed with a skin staple. The dog was allowed to recover and was returned to the owner when fully awake. Surgical resection of the mass was performed 14 days after cryoablation under general anesthesia.

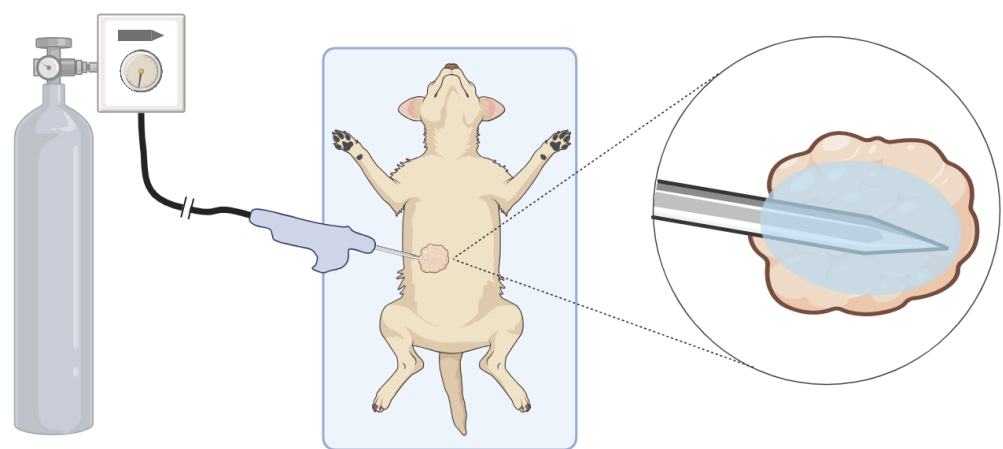


**Figure 4.** Diagram of the cryotherapy procedure setup. **Left:** the device is connected to a standard CO<sub>2</sub> tank. **Center:** the subject is sterilely draped and prepped, and the probe is inserted into the target mass. **Right:** the device is turned on and an iceball begins to grow around the probe tip inducing necrosis in the mass.

#### 2.4.2. Pathology Methods

The surgically resected tissue was fixed in 10% neutral buffered formalin and then sliced along the plane parallel to the path of probe insertion. Slides were made from paraffin-embedded tissue sections. The slides were stained with hematoxylin and eosin (H&E) and digitized for histopathological analysis. Tissue was identified as necrotic when either no viable nuclei were detected, or the cellular architecture was entirely disrupted. Regions with more than 2 nuclei present within 200  $\mu\text{m}$  were not classified as necrotic (Applied Pathology Systems, Shrewsbury, MA, USA).

### 3. Results

#### 3.1. Calorimeter Results

The average cooling power of each device, as measured over 3 trials, is shown in Table 1. The calculated surface area of the effective freezing zone for each probe was used to normalize the cooling power between devices. These data demonstrate that the CO<sub>2</sub> device generates a much greater overall cooling power. However, when normalized over the surface area of the effective freezing zone, the two cooling powers become more comparable. The argon device has a higher cooling power per unit surface area.

**Table 1.** Comparison of normalized and overall cooling power between the CO<sub>2</sub> device and the argon device.

	CO <sub>2</sub> Device	Argon Device
Cooling Power	116.9 W	27.7 W
Effective Surface Area	581.6 mm <sup>2</sup>	87.4 mm <sup>2</sup>
Normalized Cooling Power	0.20 W/mm <sup>2</sup>	0.32 W/mm <sup>2</sup>

3.2. Temperature Distribution Results

The temperature values measured by each of the four thermocouples at distance *r* from the probe surface are shown in Figure 5. The mean and 95% confidence intervals of the temperatures reached by each thermocouple at the end of the testing periods are shown in Table 2. The temperatures at 7 mm from each probe surface (corresponding to an overall diameter of 18.2 mm and 15.5 mm for the CO<sub>2</sub> and argon devices, respectively) reached similar temperature values at the end of the testing periods. For the CO<sub>2</sub> device, the final average temperature at 7 mm from the probe surface was −20.09 °C, while for the argon device, the temperature was −20.90 °C. Figure 6 shows the iceballs that were generated by each device during testing.

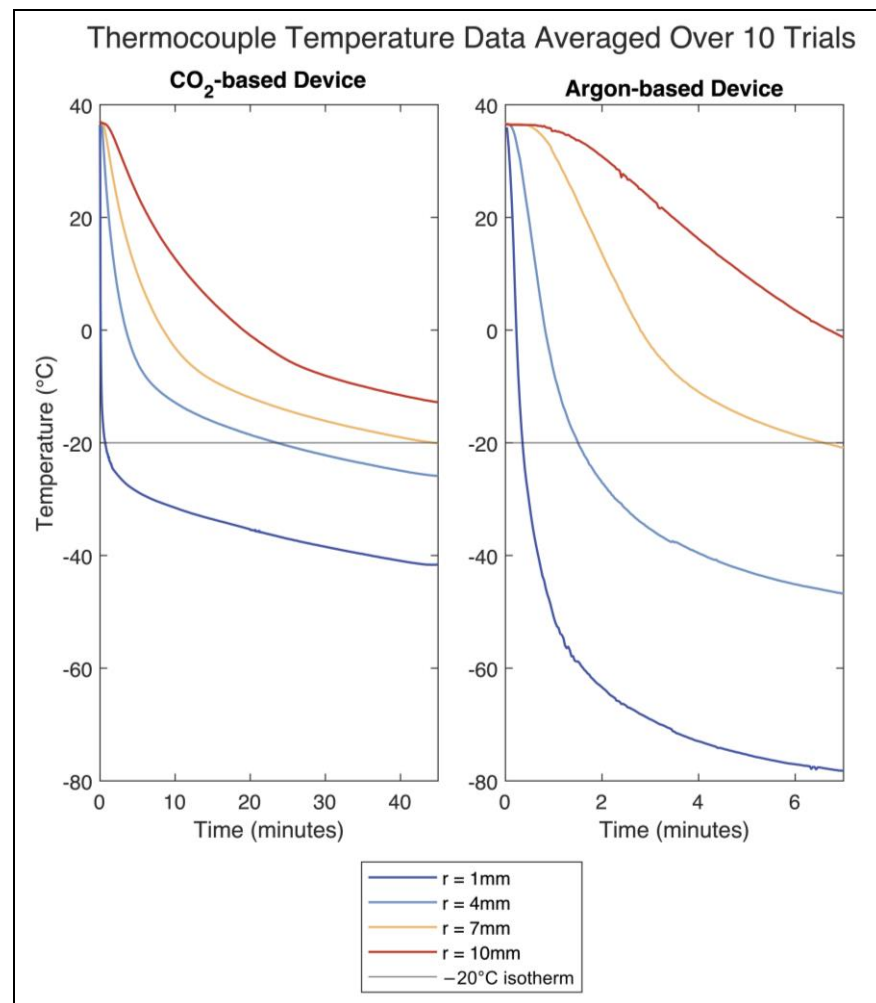


**Figure 5.** Temperature data on tissue phantom during the testing period averaged over 10 trials. *r* represents the distance of the thermocouple from the probe surface.

**Table 2.** Mean temperature with 95% confidence intervals of each thermocouple at the end of the testing period for each device.

Thermocouple Location	CO <sub>2</sub> (°C)	Argon (°C)
1 mm	−41.62 ± 1.31	−78.19 ± 3.19
4 mm	−25.89 ± 0.60	−46.76 ± 6.79
7 mm	−20.09 ± 0.57	−20.90 ± 2.28
10 mm	−12.81 ± 0.58	−1.30 ± 3.376

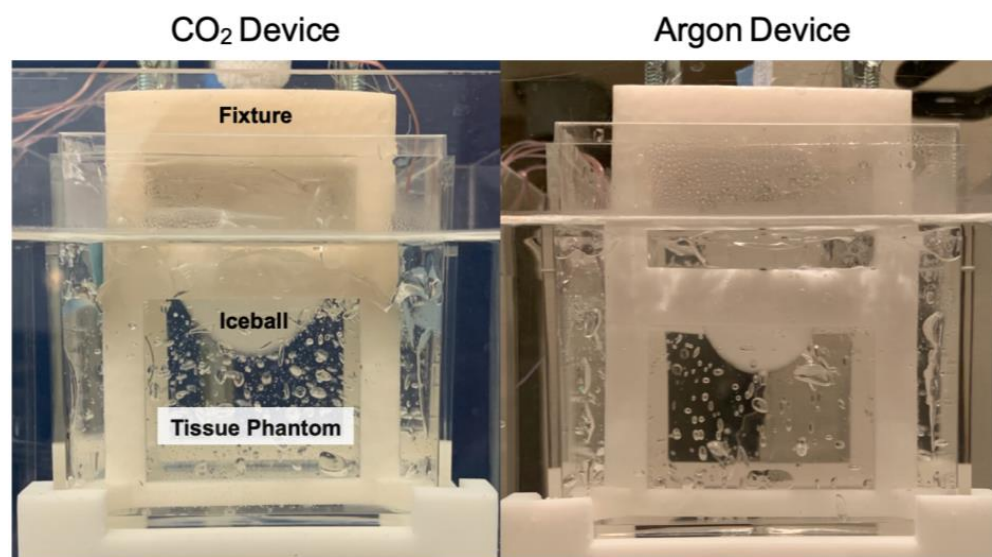


**Figure 6.** Photograph of iceballs generated during testing in the tissue phantom. **Left:** CO<sub>2</sub> probe; **right:** benchmark argon probe.

The distance of the  $-20\text{ }^{\circ}\text{C}$  isotherm from the surface of each probe was determined using a logarithmic curve fit (Equation (4)) of the thermocouple data to represent the expected theoretical heat distribution (Figure 7). For the CO<sub>2</sub> device, the distance of the  $-20\text{ }^{\circ}\text{C}$  isotherm was 6.3 mm after 45 min, and for the argon device, the distance was 6.9 mm after 7 min. Accounting for the difference in probe sizes, the overall diameters of the  $-20\text{ }^{\circ}\text{C}$  isotherm for the CO<sub>2</sub> and argon devices were 16.7 mm and 15.3 mm, respectively (Figure 8).

The coefficient values  $C_1$  and  $C_2$  of the logarithmic curves (Equation (4)) used to fit the average temperature data of each device were calculated with 95% confidence intervals. For the CO<sub>2</sub> device, the coefficients were 12.03 [8.18, 15.88] and  $-42.05$  [ $-48.44$ ,  $-35.66$ ]. For the benchmark device, the coefficients were 32.16 [11.03, 53.29] and  $-82.09$  [ $-117.1$ ,  $-47.03$ ].

The goodness-of-fit of the curves was evaluated by calculating the coefficient of determination ( $R^2$ ) and the standard error (RMSE). For the CO<sub>2</sub> device, the  $R^2$  was 0.99, and the standard error was  $1.57\text{ }^{\circ}\text{C}$ . For the benchmark device, the  $R^2$  was 0.96, and the standard error was  $8.61\text{ }^{\circ}\text{C}$ .

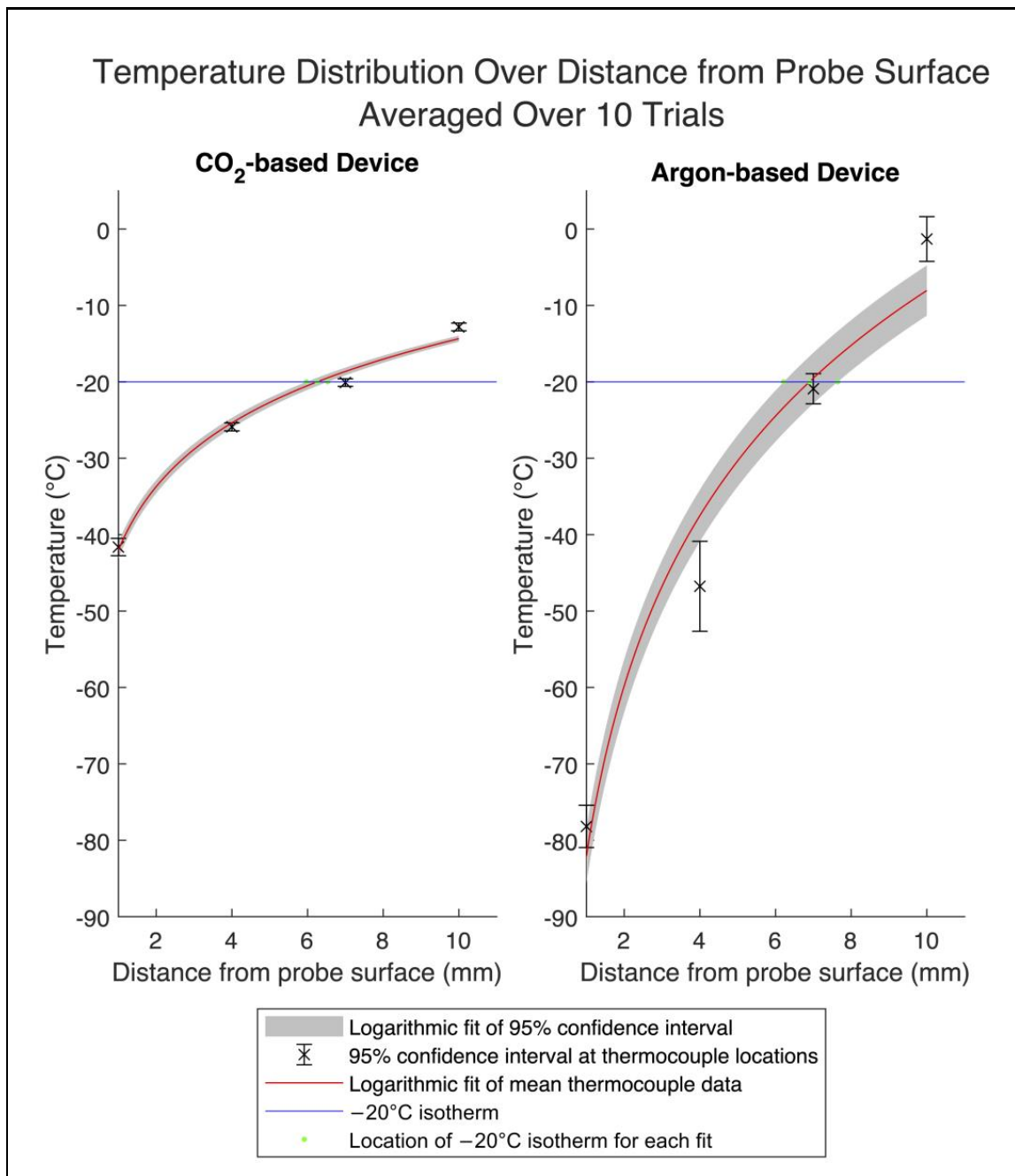


**Figure 7.** Means and 95% confidence intervals of the radial temperature distribution from the surface of the probes at the end of the testing period for each device. The red line plots the logarithmic fit of the mean thermocouple data over 10 trials. The gray area represents the 95% confidence interval of the thermocouple data fitted to a logarithmic equation. The distance of the  $-20\text{ }^{\circ}\text{C}$  isotherm from the surface of the probe with the 95% confidence interval is 6.3 mm (5.9, 6.6) for the  $\text{CO}_2$  device and 6.9 mm (6.1, 7.7) for the benchmark argon device.

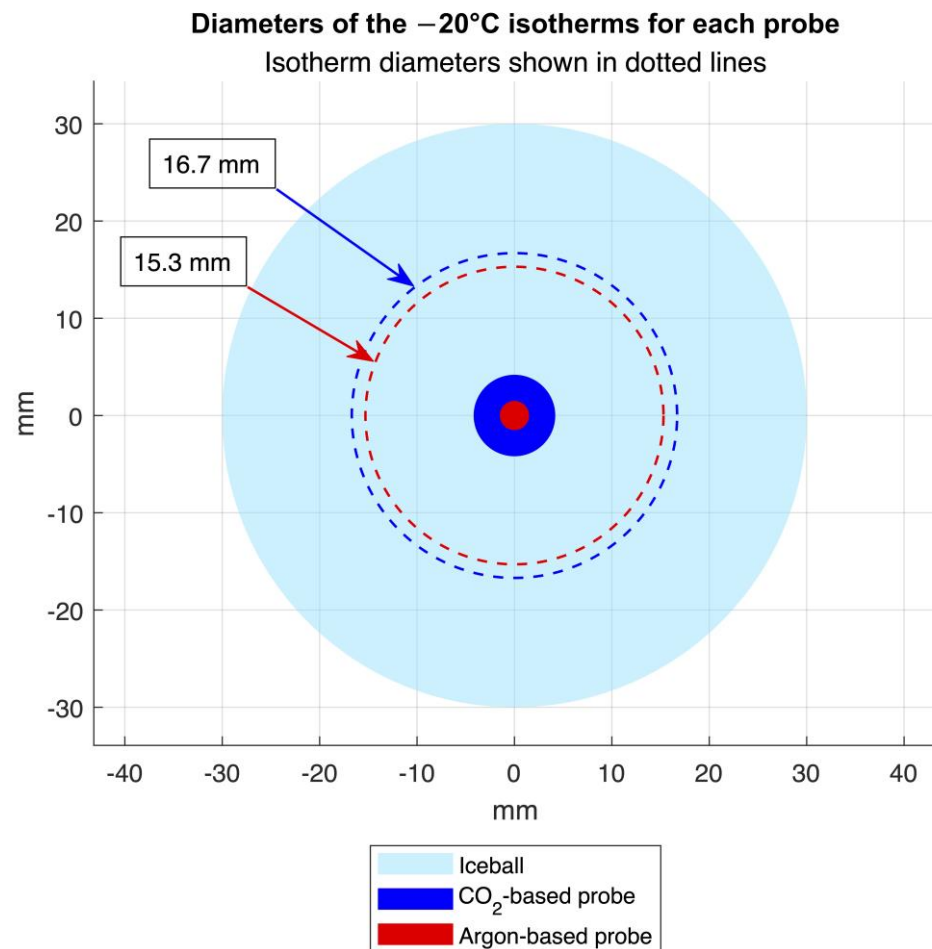


**Figure 8.** Cross-sectional representation of the probe diameters and the mean diameters of the  $-20^{\circ}\text{C}$  isotherms for each probe during testing, extrapolated from the interpolated isotherm radii, assuming radial symmetry around the probe axis. Iceball size is representative.

### 3.3. Histopathology Results

Figure 9 shows a photomicrograph of the H&E staining with the position of the CO<sub>2</sub> cryoprobe during treatment. Because of the size limit on the pathology slides used, the tissue sample was divided into two sections for embedding and then digitally reconstructed based on reference images of the fresh tissue sample immediately after resection. The pixel size of both digital images was normalized, and the aspect ratio was kept constant during reconstruction (Applied Pathology Systems). Due to the tissue fixation and reconstruction process, some of the original tissue was lost along the length of the probe track. The maximum length of necrosis along the probe track, not including areas of tissue loss, was measured to be 12.87 mm. The widest diameter of necrosis perpendicular to the probe track was measured to be 15.74 mm. Additionally, 61% of the tumor area was identified as necrotic, indicating extensive necrosis [30]. Representative areas of necrotic tissue and viable tumor tissue are shown in Figure 10.

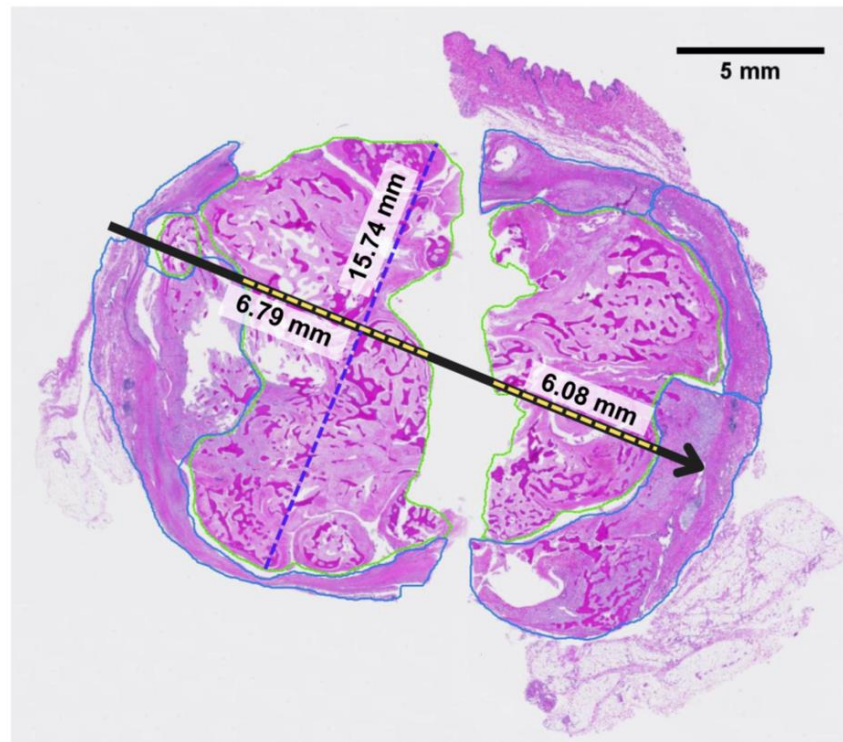


**Figure 9.** Reconstructed photomicrograph from two pieces of the mass containing annotations that show the cryoprobe orientation (black arrow). The region of necrotic tissue is outlined in green, the region of viable tumor tissue in blue, and the maximum length) and width of necrosis relative to the probe track are identified by the yellow and blue dashed lines, respectively. Length measurements do not include regions without tissue between the two pieces.

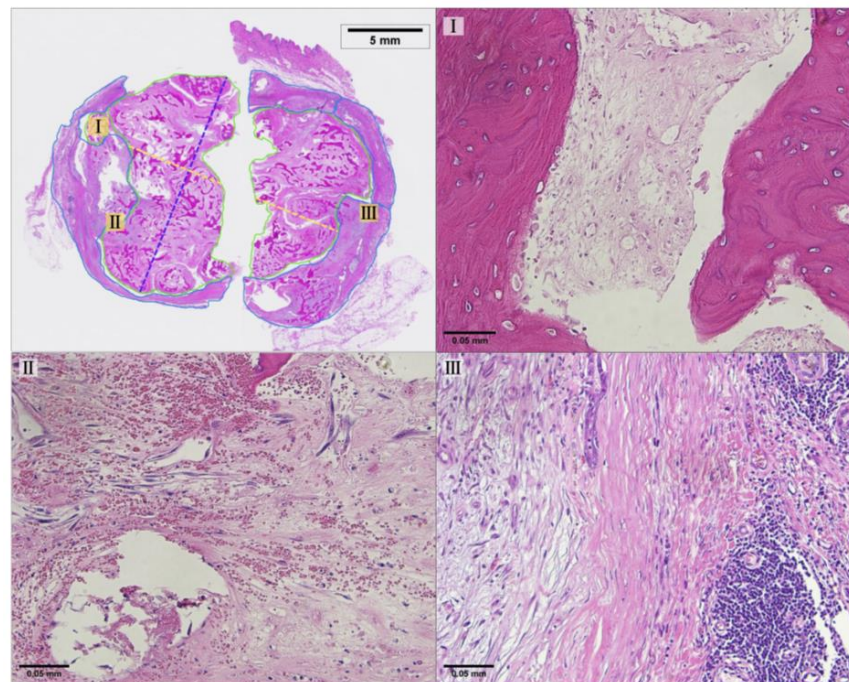


**Figure 10.** Representative regions of the treated mass showing necrotic and viable tumor tissue at 20× magnification. Region I shows necrotic tissue; region II shows the borderline between necrotic and viable tumor tissue; and region III shows viable tumor tissue. The location of each magnified region is noted on the whole slide image (top left).

#### 4. Discussion

Several prior research studies have correlated the size of the  $-20\text{ }^{\circ}\text{C}$  isotherm with the cytotoxic zone and observed margins of necrosis [23–25]. However, these studies have used argon and liquid nitrogen cryotherapy devices for treatment or have performed the tests in ex vivo tissue and therefore do not precisely capture the cell death mechanisms that occur during a low-freeze-rate cryotherapy procedure. While temperatures below  $-50\text{ }^{\circ}\text{C}$  can induce cell death very quickly, holding tissue at higher temperatures of around  $-20\text{ }^{\circ}\text{C}$  for longer periods of time can destroy tissue through cellular dehydration and recrystallization [31,32].

The lethal temperature zone of a high-freeze-rate cryotherapy device was confirmed in the argon-based device in tissue phantom testing, where a  $\sim 1.5\text{ cm}$  diameter  $-20\text{ }^{\circ}\text{C}$  isotherm was formed in under 10 min. This corresponds to the indications of use for the argon-based device, which specify a lethal zone of 1.5 cm in diameter over a 10 min treatment time [26].

Because of argon's lower boiling point and higher working pressure as compared to  $\text{CO}_2$ , it was anticipated that the argon device would significantly outperform the  $\text{CO}_2$  device when measured using a calorimeter. Although the argon device did show a marginally higher cooling power than the  $\text{CO}_2$  device when normalized by the active freezing surface area of the probe, the  $\text{CO}_2$  device demonstrated an overall cooling power of 116.9 W, a significant difference compared to the 27.7 W observed with the argon device (Table 1).

Despite the  $\text{CO}_2$  device having over 4 times the overall cooling power load compared to the argon device, the temperature profile data indicate that the argon device established a 1.5 cm diameter  $-20\text{ }^{\circ}\text{C}$  isotherm much faster than the  $\text{CO}_2$  device (Figure 5). The difference in cooling times when compared to cooling power could be attributed to variations in thermal contact resistance between the probes as well as to the latent heat dynamics of iceball formation. Factors like the contact pressure, surface area, and thermophysical and mechanical properties of the probe materials could contribute to differences in thermal contact resistance, affecting the efficiency of heat transfer [33]. Latent heat is an important factor in iceball formation as it determines the amount of cooling energy required to form ice as the iceball grows. The latent heat of fusion for the ultrasound gel tissue phantom was estimated to be  $259\text{ J/g}$  [34]. As the iceball radius expands, the cubic increase in ice volume demands exponentially more heat removal for continued growth. The  $\text{CO}_2$  device's larger probe diameter means that its iceball has a larger initial radius than that of the argon device. This introduces a more significant latent heat barrier, requiring more cooling power for the liquid-to-solid phase change. Consequently, less cooling power is directed towards decreasing the overall temperature, resulting in slower iceball growth and a longer time to generate a  $-20\text{ }^{\circ}\text{C}$  isotherm. These insights underscore the importance of a comprehensive evaluation of a cryotherapy probe beyond calorimetry for predicting practical temperature performance.

While the  $\text{CO}_2$  device took longer to generate a comparably sized lethal isotherm in relation to the argon device, it exhibited a significantly narrower temperature range in benchtop testing, and it also demonstrated reduced variability in temperature measurements (Table 2). A primary metric controlling the individual performance of a cryotherapy device is the pressure of the incoming gas. Because of argon's higher cryogenic potential, the gas pressure can be downregulated during use.  $\text{CO}_2$ , as a weaker cryogen, requires the full working pressure of a standard  $\text{CO}_2$  tank to achieve similar cooling outcomes. When using the  $\text{CO}_2$  cryotherapy device, the supplying gas tank is thermally regulated to achieve a stable starting pressure of  $970 \pm 30\text{ psi}$ , and a constant heat load is applied to the gas tank during use. This consistent approach ensures a uniform pressure drop for  $\text{CO}_2$  across multiple trials, albeit resulting in a gradual performance decline over time. In contrast, the direct pressure regulation of argon gas introduces irregular fluctuations in gas flow rate, potentially contributing to greater temperature variation across trials [35].

It is worth noting that this study did not explore the differences in variability between the two devices, though it presents a compelling area for future research. Additional studies

may yield a deeper understanding of the factors contributing to temperature variation and their implications for diverse cryotherapy devices and applications.

The benchtop tissue phantom studies have established that the CO<sub>2</sub> device can generate a comparable temperature profile to the benchmark argon device. While there is a significant difference in the time taken for each device to reach  $-20\text{ }^{\circ}\text{C}$  at a 1.5 cm diameter in the benchtop trials, the variability in thermal and mechanical properties between different tissue types makes it difficult to directly correlate the size and time efficiency of experimental isotherm results to *in vivo* performance. Therefore, the treatment time for the CO<sub>2</sub> device is not determined by the time to reach a 1.5 cm diameter  $-20\text{ }^{\circ}\text{C}$  isotherm as measured in bench testing. Because of the complex physiological thermal effects on freezing performance, dosage times similar to those that are used in conventional cryotherapy treatments were used for the CO<sub>2</sub> device. Based on the results of prior animal studies, a standard treatment time consisting of two 10 min freezes separated by a 7 min thaw was deemed appropriate for this *in vivo* treatment. This treatment time is significantly shorter than the 45 min it took for the device to reach a 1.5 cm diameter  $-20\text{ }^{\circ}\text{C}$  isotherm during bench testing.

It should be noted that there are multiple factors that can cause tissue shrinkage between the time of cryotherapy treatment and the histopathological analysis of necrosis margins. After undergoing the cryotherapy procedure, excision of the treated mass was not performed until 2 weeks later. During this period, the breakdown and remodeling of necrotic tissue with fibrotic replacement is expected, leading to an overall reduction in tissue dimensions [32,36,37]. Additionally, after the mass was resected and cut into sections for analysis, the tissue sections were fixed with formalin, which can result in tissue shrinkage of 10% or more [38,39]. Due to the complex processes underlying these shrinkage factors, it is difficult to accurately quantify the level of shrinkage that occurred. As a result, it is likely that the true margin of necrosis in the body during treatment exceeds the measurement obtained through pathological analysis.

As shown in the *in vivo* study, the diameter of necrosis after 20 min of freezing, i.e., two 10 min freezes, with the CO<sub>2</sub> device was 1.57 cm. The temperature data for the CO<sub>2</sub> device show that after 20 min of freezing in the benchtop tissue phantom, the  $-20\text{ }^{\circ}\text{C}$  isotherm had a diameter of less than 1.2 cm. On the bench, the  $-20\text{ }^{\circ}\text{C}$  isotherm generated by the CO<sub>2</sub> device took around 30 min to reach a 1.57 cm diameter. This suggests that the mechanisms of cell death associated with “slow” cryotherapy treatment, such as increased cellular dehydration and recrystallization, allow for a larger area of necrosis than predicted by bench test results.

While this study is limited in that only a single *in vivo* treatment was performed, the histopathology results combined with the benchtop comparison data provide strong evidence for the feasibility of CO<sub>2</sub> cryotherapy as a treatment for breast cancer in low-resource settings. This research has significant implications for the development of CO<sub>2</sub> cryotherapy through additional *in vivo* studies for eventual implementation in human healthcare applications. The comparison between the *in vivo* necrosis margins and the  $-20\text{ }^{\circ}\text{C}$  isotherm size over similar periods of freezing also reveals a potential area of investigation of the unique impacts of slow-cryotherapy that occur when using CO<sub>2</sub> to induce cryogenic temperatures and activate cell death pathways. Further development could allow for the low-cost and effective treatment of breast cancer in low-resource regions where access to advanced treatment options is limited.

The evaluation of CO<sub>2</sub> cryotherapy in comparison with a commercially available argon device, along with its demonstrated viability to induce necrosis in clinically relevant volumes of cancerous tissue in spontaneously occurring tumors in a large animal model within a standard treatment time, presents a promising outlook for the application of CO<sub>2</sub> cryotherapy in human treatment. Characterized by low cost and minimal resource requirements, CO<sub>2</sub> cryotherapy is a compelling option for cancer treatment in low-resource settings and is well-positioned to address a growing disparity in global breast cancer care.

**Author Contributions:** Conceptualization, methodology, Y.H., N.G., D.L.K. and B.S.; formal analysis, Y.H., N.G. and K.O.; investigation, Y.H., N.G., K.O. and D.L.K.; resources, D.L.K., N.J.D. and B.S.; writing—original draft preparation, Y.H., N.G. and K.O.; writing—review and editing, Y.H., N.G., D.L.K., N.J.D. and B.S.; project administration, B.S.; funding acquisition, Y.H. and B.S. All authors have read and agreed to the published version of the manuscript.

**Funding:** This research was supported by NIH/NCI grant number R43-CA261360-01A1.

**Institutional Review Board Statement:** The animal study protocol was approved by the Animal Care and Use Committee of Johns Hopkins University (protocol code DO21M438, date of approval 1 February 2022).

**Informed Consent Statement:** Not applicable.

**Data Availability Statement:** Data will be made available upon request.

**Acknowledgments:** We would like to acknowledge Kathleen Gabrielson for her histopathology assistance, Kristen Kellar-Graney for her coordination of the study's subject recruitment, Cheri Rice for her veterinary technician services, and Applied Pathology Systems for their pathology analysis services.

**Conflicts of Interest:** Y.H., B.S., and N.J.D. are inventors of the patent-pending CO<sub>2</sub>-based cryotherapy device (WO2019213205A1) described in this work. Y.H., B.S., N.G., and K.O. are employed by Kubanda Cryotherapy. The remaining authors declare that the research was conducted in the absence of any commercial relationships that could be construed as a potential conflict of interest. The funders had no role in the design of the study; in the collection, analyses, or interpretation of data; in the writing of the manuscript; or in the decision to publish the results.

## References

1. Al-Sukhun, S.; Tbaishat, F.; Hammad, N. Breast cancer priorities in limited-resource environments: The price-efficacy dilemma in cancer care. *Am. Soc. Clin. Oncol. Educ. Book* **2022**, *42*, 416–422. [CrossRef] [PubMed]
2. Francies, F.Z.; Hull, R.; Khanyile, R.; Dlamini, Z. Breast Cancer in Low-Middle Income Countries: Abnormality in Splicing and Lack of Targeted Treatment Options. Available online: <https://www.ncbi.nlm.nih.gov/pmc/articles/PMC7269781/> (accessed on 25 December 2023).
3. Arnold, M.; Morgan, E.; Rungay, H.; Mafra, A.; Singh, D.; Laversanne, M.; Vignat, J.; Gralow, J.R.; Cardoso, F.; Siesling, S.; et al. Current and Future Burden of Breast Cancer: Global Statistics for 2020 and 2040. *Breast* **2022**, *66*, 15–23. [CrossRef] [PubMed]
4. Moo, T.-A.; Sanford, R.; Dang, C.; Morrow, M. Overview of Breast Cancer Therapy. *PET Clin.* **2018**, *13*, 339–354. [CrossRef] [PubMed]
5. GlobalSurg Collaborative; National Institute for Health Research Global Health Research Unit on Global Surgery. Global variation in postoperative mortality and complications after cancer surgery: A multicentre, prospective cohort study in 82 countries. *Lancet* **2021**, *397*, 387–397. [CrossRef] [PubMed]
6. Cardone, C.; Arnold, D. The Cancer Treatment Gap in Lower- to Middle-Income Countries. *Oncology* **2023**, *101* (Suppl. S1), 2–4. [CrossRef] [PubMed]
7. Elmore, S.N.; Polo, A.; Bourque, J.-M.; Pynda, Y.; van der Merwe, D.; Grover, S.; Hopkins, K.; Zubizarreta, E.; Abdel-Wahab, M. Radiotherapy Resources in Africa: An International Atomic Energy Agency Update and Analysis of Projected Needs. *Lancet Oncol.* **2021**, *22*, e391–e399. [CrossRef]
8. Shah, S.C.; Kayamba, V.; Peek, R.M.; Heimburger, D. Cancer Control in Low- and Middle-Income Countries: Is It Time to Consider Screening? *J. Glob. Oncol.* **2019**, *5*, 1–8. [CrossRef]
9. Donkor, A.; Atuwu-Ampoh, V.D.; Yakanu, F.; Torgbenu, E.; Ameyaw, E.K.; Kitson-Mills, D.; Vanderpuye, V.; Kyei, K.A.; Anim-Sampong, S.; Khader, O.; et al. Financial Toxicity of Cancer Care in Low- and Middle-Income Countries: A Systematic Review and Meta-Analysis. *Support. Care Cancer* **2022**, *30*, 7159–7190. [CrossRef] [PubMed]
10. Newman, L.A. Breast cancer screening in low and middle-income countries. *Best Pract. Res. Clin. Obstet. Gynaecol.* **2022**, *83*, 15–23. [CrossRef]
11. Ferlic, D.J.; Kotula, F.T.; Amplatz, K. Mammography Apparatus. U.S. Patent 4901335, 13 February 1990.
12. Souney, S.; Roeder, R. Portable Hand-Carry Satellite Diagnostic Ultrasound System for General and Cardiac Imaging. U.S. Patent US20020040186A1, 12 November 2002.
13. Tran, T.T.; Hlaing, M.; Krause, M. Point-of-Care Ultrasound: Applications in Low- and Middle-Income Countries. *Curr. Anesthesiol. Rep.* **2021**, *11*, 69–75. [CrossRef]
14. Becker, D.M.; Tafoya, C.A.; Becker, S.L.; Kruger, G.H.; Tafoya, M.J.; Becker, T.K. The Use of Portable Ultrasound Devices in Low- and Middle-income Countries: A Systematic Review of the Literature. *Trop. Med. Int. Health* **2016**, *21*, 294–311. [CrossRef] [PubMed]

15. Bhimani, F.; Zhang, J.; Shah, L.; McEvoy, M.; Gupta, A.; Pastoriza, J.; Shihabi, A.; Feldman, S. Can the clinical utility of ibreastexam, a novel device, aid in optimizing breast cancer diagnosis? A systematic review. *JCO Glob. Oncol.* **2023**, *9*, e2300149. [[CrossRef](#)] [[PubMed](#)]
16. Mokbel, K.; Kodresko, A.; Ghazal, H.; Mokbel, R.; Trembley, J.; Jouhara, H. The Evolving Role of Cryosurgery in Breast Cancer Management: A Comprehensive Review. *Cancers* **2023**, *15*, 4272. [[CrossRef](#)] [[PubMed](#)]
17. Mohammed, A.; Miller, S.; Douglas-Moore, J.; Miller, M. Cryotherapy and Its Applications in the Management of Urologic Malignancies: A Review of Its Use in Prostate and Renal Cancers. *Urol. Oncol. Semin. Orig. Investig.* **2014**, *32*, e19–e39. [[CrossRef](#)] [[PubMed](#)]
18. Winkle, R.A.; Mead, R.H.; Engel, G.; Kong, M.H.; Patrawala, R.A. Physician-controlled costs: The choice of equipment used for atrial fibrillation ablation. *J. Interv. Card. Electrophysiol.* **2013**, *36*, 157–165. [[CrossRef](#)] [[PubMed](#)]
19. Bang, H.J.; Littrup, P.J.; Goodrich, D.J.; Currier, B.P.; Aoun, H.D.; Heilbrun, L.K.; Vaishampayan, U.; Adam, B.; Goodman, A.C. Percutaneous cryoablation of metastatic renal cell carcinoma for local tumor control: Feasibility, outcomes, and estimated cost-effectiveness for palliation. *J. Vasc. Interv. Radiol.* **2012**, *23*, 770–777. [[CrossRef](#)] [[PubMed](#)]
20. Sprenkle, P.C.; Mirabile, G.; Durak, E.; Edelstein, A.; Gupta, M.; Hruby, G.W.; Okhunov, Z.; Landman, J. The Effect of Argon Gas Pressure on Ice Ball Size and Rate of Formation. *J. Endourol.* **2010**, *24*, 1503–1507. [[CrossRef](#)] [[PubMed](#)]
21. Cooper, S.M.; Dawber, R.P. The history of cryosurgery. *J. R. Soc. Med.* **2001**, *94*, 196–201. [[CrossRef](#)]
22. Surtees, B.; Young, S.; Hu, Y.; Wang, G.; McChesney, E.; Kuroki, G.; Acree, P.; Thomas, S.; Blair, T.; Rastogi, S.; et al. Validation of a low-cost, carbon dioxide-based cryoablation system for percutaneous tumor ablation. *PLoS ONE* **2019**, *14*, e0207107. [[CrossRef](#)]
23. Hinshaw, J.L.; Lee, F.T.; Laeseke, P.F.; Sampson, L.A.; Brace, C. Temperature isotherms during pulmonary cryoablation and their correlation with the zone of ablation. *J. Vasc. Interv. Radiol.* **2010**, *21*, 1424–1428. [[CrossRef](#)]
24. Snyder, K.K.; Van Buskirk, R.G.; Baust, J.G.; Baust, J.M. Breast cancer cryoablation: Assessment of the impact of fundamental procedural variables in an in vitro human breast cancer model. *Breast Cancer Basic Clin. Res.* **2020**, *14*, 117822342097236. [[CrossRef](#)]
25. Littrup, P.J.; Freeman-Gibb, L.; Andea, A.; White, M.; Amerikia, K.C.; Bouwman, D.; Harb, T.; Sakr, W. Cryotherapy for breast fibroadenomas. *Radiology* **2005**, *234*, 63–72. [[CrossRef](#)]
26. Boston Scientific Corporation. Classic Needle Sell Sheet. Boston Scientific Corporation: Marlborough, MA, n.d. Available online: [https://www.bostonscientific.com/content/dam/bostonscientific/pi/portfolio-group/cryoablation/visualice/Classic\\_Needle\\_Sell\\_Sheet.pdf](https://www.bostonscientific.com/content/dam/bostonscientific/pi/portfolio-group/cryoablation/visualice/Classic_Needle_Sell_Sheet.pdf) (accessed on 26 February 2024).
27. Savitzky, A.; Golay, M.J. Smoothing and differentiation of data by simplified least squares procedures. *Anal. Chem.* **1964**, *36*, 1627–1639. [[CrossRef](#)]
28. Hossain, S.; Mohammadi, F. One-dimensional Steady-state Analysis of Bioheat Transfer Equation: Tumour Parameters Assessment for Medical Diagnosis Application. In Proceedings of the IMETI 2013-6th International Multi-Conference on Engineering and Technological Innovation, Orlando, FL, USA, 9–12 July 2013; Proceedings 2013. pp. 26–30.
29. Parsons, K.; Reichanadter, T.; Vicksman, A.; Segur, H. Explicit solution for cylindrical heat conduction. *Am. J. Undergrad. Res.* **2016**, *13*, 109. [[CrossRef](#)]
30. Pollheimer, M.J.; Kornprat, P.; Lindtner, R.A.; Harbaum, L.; Schlemmer, A.; Rehak, P.; Langner, C. Tumor necrosis is a new promising prognostic factor in colorectal cancer. *Hum. Pathol.* **2010**, *41*, 1749–1757. [[CrossRef](#)]
31. Theodorescu, D. Cancer cryotherapy: Evolution and biology. *Rev. Urol.* **2004**, *6* (Suppl. S4), S9–S19.
32. Mazur, P. Physical-chemical factors underlying cell injury in cryosurgical freezing. In *Cryosurgery*; Rand, R., Rinfret, A., von Leden, H., Eds.; Charles C. Thomas: Springfield, IL, USA, 1968; pp. 32–51.
33. Salmon, K.; Nellis, G.; Pfothenhauer, J. Experimental characterization of cryogenic contact resistance. *Cryogenics* **2022**, *128*, 103587. [[CrossRef](#)]
34. Etheridge, M.L.; Choi, J.; Ramadhyani, S.; Bischof, J.C. Methods for characterizing convective cryoprobe heat transfer in Ultrasound Gel Phantoms. *J. Biomech. Eng.* **2013**, *135*, 021002. [[CrossRef](#)]
35. Understanding the Characteristics of Pressure Regulators. Available online: <https://fluidpowerjournal.com/understanding-the-characteristics-of-pressure-regulators/> (accessed on 28 December 2023).
36. Erinjeri, J.P.; Clark, T.W.I. Cryoablation: Mechanism of action and Devices. *J. Vasc. Interv. Radiol.* **2010**, *21* (Suppl. S8), S187–S191. [[CrossRef](#)] [[PubMed](#)]
37. Kwak, K.; Yu, B.; Lewandowski, R.J.; Kim, D.-H. Recent progress in cryoablation cancer therapy and nanoparticles mediated cryoablation. *Theranostics* **2022**, *12*, 2175–2204. [[CrossRef](#)] [[PubMed](#)]
38. Tran, T.; Sundaram, C.P.; Bahler, C.D.; Eble, J.N.; Grignon, D.J.; Monn, M.F.; Simper, N.B.; Cheng, L. Correcting the shrinkage effects of formalin fixation and tissue processing for renal tumors: Toward standardization of pathological reporting of Tumor Size. *J. Cancer* **2015**, *6*, 759–766. [[CrossRef](#)]
39. Upchurch, D.A.; Klocke, E.E.; Henningson, J.N. Amount of skin shrinkage affecting tumor versus grossly normal marginal skin of dogs for cutaneous mast cell tumors excised with curative intent. *Am. J. Vet. Res.* **2018**, *79*, 779–786. [[CrossRef](#)]

**Disclaimer/Publisher’s Note:** The statements, opinions and data contained in all publications are solely those of the individual author(s) and contributor(s) and not of MDPI and/or the editor(s). MDPI and/or the editor(s) disclaim responsibility for any injury to people or property resulting from any ideas, methods, instructions or products referred to in the content.